Classification:

BIOLOGICAL SCIENCES: Neuroscience; PHYSICAL SCIENCES: Engineering;

Transcranial *in vivo* recording of neural activity in the rodent brain with near-infrared photoacoustic voltage-sensitive dye imaging

Jeeun Kang[a], Haichong K. Zhang[a], Shilpa D. Kadam[b], Fedorko Julie[c], Heather Valentine[c], Ping Yan[d], Jin U. Kang[a], Arman Rahmim[c], Albert Gjedde[c,e], Leslie M. Loew[d], Dean F. Wong[c,e,f,g,h], Emad M. Boctor[a,c,*]

[a] Whiting School of Engineering, Johns Hopkins University, Baltimore, MD 21218, USA
[b] Department of Neurology and Neurosurgery, Hugo W. Moser Research Institute at Kennedy Krieger, Johns Hopkins Medical Institutions, Baltimore, MD 21205, USA
[c] Russell H. Morgan Department of Radiology and Radiological Science, Johns Hopkins Medical Institutions, Baltimore, MD 21287, USA
[d] Department of Cell Biology, University of Connecticut Health, Farmington, CT 06030, USA
[e] Department of Neuroscience, University of Copenhagen, Copenhagen 2200, Denmark
[f] Solomon H. Snyder Department of Neuroscience, Johns Hopkins Medical Institutions, Baltimore, MD 21205, USA
[g] Department of Psychiatry and Behavioral Sciences, Johns Hopkins Medical Institutions, Baltimore, MD 21287, USA
[h] Department of Neurology, Johns Hopkins Medical Institutions, Baltimore, MD 21205, USA

Corresponding author:
*Emad M. Boctor, PhD
Johns Hopkins Outpatient Center
601 N. Caroline St.,
Baltimore, MD 21287
Office: +1 (443) 287-2975
Email: eboctor1@jhmi.edu

Short title: Photoacoustic recording of neural activity *in vivo*

Abstract

Minimally-invasive monitoring of electrophysiological neural activities in real-time—that would enable quantification of neural functions without a need for invasive craniotomy and the longer time constants of fMRI and PET—presents a very challenging yet significant task for neuroimaging. We present *in vivo* proof-of-concept results of transcranial photoacoustic (PA) imaging of chemoconvulsant seizure activity in the rat brain. The framework involves use of a fluorescence quenching-based near-infrared voltage-sensitive dye (VSD) delivered through the blood-brain barrier (BBB), opened by pharmacological modulation of adenosine receptor signaling. Using normalized time-frequency analysis on temporal PA sequences, the neural activity in the seizure group was distinguished from those of the control groups. Electroencephalogram (EEG) recording confirmed the changes of severity and frequency of brain activities, induced by chemoconvulsant seizures of the rat brain. The findings demonstrate that PA imaging of fluorescence quenching-based VSD is a promising tool for *in vivo* recording of deep brain activities in the rat brain, thus excluding the use of invasive craniotomy.

Keywords: photoacoustics; brain imaging; fluorescence quenching; near-infrared; voltage-sensitive dye; chemoconvulsant seizure; rat brain; millisecond time resolution

Significance statement: Minimally-invasive imaging of electrophysiological brain activity in real-time (order of milliseconds) represents a significant challenge with existing neuroimaging modalities. This is because existing imaging modalities do not have sufficient transcranial sensitivity with the necessary temporal and spatial resolutions. Here, we present *in vivo* proof-of-concept results for real-time transcranial photoacoustic imaging of near-infrared voltage-sensitive dye (VSD) signals. The chosen VSD produces photoacoustic signals that are modulated by membrane potential. The imaging successfully detected the perturbation caused by chemoconvulsant seizures in rat brain. We introduce this novel method to the neuroscientific investigation of rodent brains, with the promise of translation into primate and human brains.

Introduction

The quantification and monitoring of brain function is a major goal of neuroscience and research into the underlying mechanisms of the working brain.(1-5) Towards this objective, several modalities have been introduced for the purpose of appropriate neuroimaging; however, existing methods have limitations. Positron emission tomography (PET) provides high molecular resolution and pharmacological specificity, but suffers from low spatial and temporal resolution.(6-8) Functional magnetic resonance imaging (fMRI) provides higher spatial resolution of brain activity; however, the record is a complex blood-oxygenation level dependent (BOLD) signal with comparatively low temporal resolution and uncertain interpretation. (9, 10) Optical imaging approaches have been used to monitor the brain function of small animals but have limited dynamic ranges and cover only superficial tissue depths because of light scattering and absorbance during penetration of biological tissue *in vivo*.(11, 12) The approaches require invasive craniotomy, with problematic long-term consequences such as dural regrowth, greater likelihood of inflammatory cascade initiation, and lack of practicality of translation to non-human primate and ultimately to human studies, including neuropsychiatric disorders.(13) In addition, real-time imaging simultaneously with deep penetration has not been demonstrated. Near-infrared spectroscopy (NIRS) non-invasively monitors brain function in real-time (~ 1ms) for deep biological tissues (~several mm), but suffers from poor spatial resolution (~ 1 cm) at those depths.(14, 15) Therefore, minimally-invasive monitoring of electrophysiological brain activities in real-time remains a task at hand in neuroimaging, with the aim to quantify brain functions at high spatial resolution in the depths of brain tissue, without need for invasive craniotomy.

To overcome the current challenges, photoacoustic (PA) imaging has been investigated as a promising hybrid modality that provides the molecular contrast of brain function with acoustic transcranial penetration and high spatial resolution.(16, 17) In PA imaging, radio-frequency (RF) acoustic pressure is generated, depending on the thermo-elastic property and light absorbance of a target illuminated by pulsed laser, and it is detected by an ultrasound transducer. Based on this mechanism, several PA approaches to detect electrophysiological brain activities recently have been developed in both tomographic and microscopic imaging modes. Deán-Ben et al. presented *in vivo* whole brain monitoring of zebrafish using real-time PA tomography of a genetically encoded calcium indicator, GCaMP5G.(18) Ruo et al. reported PA imaging *in vivo* of mouse brain responses to electrical stimulation and 4-aminopyridine-induced epileptic seizures by means of hydrophobic anions such as dipicrylamine (DPA).(19) However, these studies used voltage sensing in the visible spectral range (488 nm and 530 nm for GCaMP5G; 500 nm and

570 nm for DPA) that is not suitable for recording of deep neural activity because of the significant optical attenuation by blood.

Here, we present transcranial recording of electrophysiological neural activity *in vivo* with near-infrared PA voltage-sensitive dye (VSD) imaging during chemoconvulsant seizures in the rat brain with intact scalp. As a step towards minimally-invasive external imaging in primates and human brains, the results demonstrate that PA imaging of fluorescence quenching-based VSD is a promising approach to the recording deep brain activities in rat brain, without need for craniotomy.

Results

We based the development of the *in vivo* PA imaging system on a 128-channel array ultrasound transducer and a Nd:YAG laser system with a tunable optical parametric oscillator (OPO) (Fig. 1a). We maintained the energy density employed in the experiments at 3.5 mJ/cm^2 that is far below the maximum permissible exposure (MPE) of skin to laser radiation of the ANSI safety standards.(20) A wavelength of 790 nm was used, at which the light energy was sufficiently absorbed by the near-infrared VSD, i.e., IR780. Probing at this wavelength avoided the undesired time-variant change of oxygen saturation, being at the isosbestic point of Hb and HbO_2 absorption spectra in the *in vivo* setup (Fig. 1b). Fig. 1c presents a representative cross-sectional PA image of a rat brain. The outlines for the brain and motor cortex were drawn based on the rat brain atlas (21) (Fig. S1). We conducted the *in vivo* experiments according to the protocol shown in Fig. 1d, with a design composed of seizure, control, and negative control groups. Seizure was not induced in the control group subject to VSD + Lexiscan administration. The negative control group served mainly to monitor the hemodynamic change induced by Lexiscan injection and seizure induction without VSD administration.

Fig. 2 demonstrates our *in vitro* experimental results using a lipid vesicle model. In the spectrophotometric measurements shown in Fig. 2a, we obtained 40.1% of fluorescence emission change with IR780 between polarized and depolarized states, with the administrations of valinomycin and gramicidin, respectively, while having only 3% of corresponding absorbance change. Based on the fluorescence quenching-based VSD mechanism, the PA intensity in the depolarization state decreased by 12.3 ± 6.7% at 790 nm, compared to the polarized state ($P = 0.044$, Fig. 2b). The theoretical model presented in a previous study suggested that the

depolarization events of the lipid vesicle changed the quantum yield of VSD by as much as 0.28 ± 0.10 in the depolarized state, from 0.17 ± 0.06 in the polarized state (Fig. S2).(22)

With the confirmation from the *in vitro* lipid vesicle model, we conducted the *in vivo* validation for transcranial sensing of electrophysiological neural activity in the rat brain according to the protocol shown in Fig. 1d. The PA probe was located on the cross-section at around the Interaural 11.2 mm, Bregma 2.2 mm to monitor the PA signal change originating from motor cortex (Fig. S1) (21), in eight-to-nine-week-old female Sprague Dawley rats anesthetized with ketamine/xylazine. A rat head was stably fixed with stereotaxic equipment, and was shaved for better acoustic/optic coupling. Movies S1, S2, and S3 present the representative temporal PA image sequence obtained during 9 to 10 min from the seizure, control, and negative control groups. To extract the seizure-induced neural activity from the PA image sequence, we used the short-time Fourier transform (STFT)-based normalized time-frequency analysis method illustrated in Fig. S3. Fig. 3a presents the representative neural activity maps projected in the temporal direction for 10 min in the seizure, control, and negative control groups. The chemoconvulsant seizures induced substantial VSD responses in both motor cortices, while control and negative control groups had consistent records throughout the baseline and comparison phases. The dynamic evolutions of neural activity map over time are presented in Movie S4, S5, and S6. In the respective STFT spectrograms obtained from the regions-of-interest (ROIs) indicated by asterisks in Fig. 3a, significant differences between seizure and control groups were also recorded (Fig. 3b). Fig. 3c shows the fractional change of the neural activity index measured from motor cortexes of each experimental group. The seizure group depicted as much as 2.4-fold higher neural activity compared to the baseline: 2.40 ± 0.42 vs. 1.00 ± 0.20 ($P < 0.0001$) that is 11.40 times more than pure VSD contrast, i.e., 12.3%. This higher contrast could be obtained by augmenting the VSD signal component at high frequency, while filtering out the stationary VSD signal components during our normalized time-frequency analysis. Otherwise, the control group indicated consistent neural activity indices compared to those in the baseline phases: 0.93 ± 0.25 vs. 1.00 ± 0.20. The negative control group demonstrated no significant interference in our neural activity sensing: 1.00 ± 0.25, 0.92 ± 0.23, 1.01 ± 0.26 for the cases of Lexiscan-/PTZ-, Lexiscan+/PTZ-, and Lexiscan+/PTZ+, respectively. The neural activity index for each rat is presented in Fig. S4.

We evaluated the efficiency of pharmacological treatment for adenosine receptor signaling modulation by monitoring the evolution of the PA intensity over time with the intravenous injection of ragadenoson (Fig. S5). The fractional increases from the natural condition (VSD-,

Lexiscan-) present statistically significant changes between groups with VSD only and VSD + Lexiscan: 1.09 ± 0.09 and 1.14 ± 0.09, respectively ($P<0.0001$ with 480 time points) that indicates the VSD penetration into the blood-brain barrier (BBB).

We validated the chemoconvulsant-induced seizure activity in the *in vivo* protocol with EEG recording. Using a well-established model of chemoconvulsant-induced *status epilepticus*, we replicated the classic evolution of chemoconvulsant-induced *status epilepticus* using PTZ (Fig. 4).(23) These evolutions as related to bursts of synchronized neural activity *in vivo* were assessed in two similar experimental protocols mirrored for the EEG and PA experiments. We recorded vEEGs of seizure inductions using PTZ (45mg/kg IP injections) in anesthetized rats. EEG baseline recording continued until a stable seizure induction profile (i.e., continuous burst discharges indicating synchronized neuronal depolarization-related action potentials) was recorded using sub-dermal EEG scalp electrodes. The seizure activity in EEG was associated with tonic-clonic movements in the fore- and hind-limbs of the anesthetized rats, indicating motor cortex involvement (Movie S4) recorded on synchronous video during EEG acquisition. The PTZ evolution of status on EEG did not alter with IV VSD treatment.

Discussion

Here, we present a transcranial PA recording of electrophysiological neural activity *in vivo* using near-infrared VSD for chemoconvulsant seizure in rat brain. In the lipid vesicle phantom experiment, the near-infrared VSD, IR780, clearly revealed the signature of the VSD mechanism in polarization/depolarization events induced by valinomycin and gramicidin (Fig. 2). The *in vivo* validation study demonstrated that the global seizure activity of the motor cortex was clearly differentiated from the activities of the control and negative control groups (Fig. 3, Movie S5, S6, S7). The results also closely agreed with the electrophysiological activities observed by EEG measurement, with an identical experimental setup and protocol (Fig. 4).

The potentially confounding factors in the experimental setup and protocol employed need to be carefully considered and eliminated. The change in cerebral blood volume (CBV) during chemoconvulsant seizure can generate fluctuations of PA intensity over time that can be misinterpreted as the suppressive VSD response.(24-26) To address this concern, we adjusted two considerations in the *in vivo* protocol and analysis: (1) we allocated 5-10 min of the time duration for hemodynamic stabilization before collecting the PA data, and (2) normalized the STFT spectrogram in both the frequency and time dimensions. Zhang et al. suggested that the

total hemoglobin began to change in the pre-ictal period and remained stable after the initiation of tonic-clonic seizure, and the time length from PTZ injection to seizure onset was ~2 min on average,(27) but it was sufficiently covered by our stabilization period in the *in vivo* protocol. The neural activity map could be stabilized with respect to the CBV change, because the bias on the STFT spectrogram could be rejected during normalization procedures. The negative control group in our *in vivo* protocol is mainly served to test whether these considerations successfully would work. The PA data obtained without any VSD administration went through an identical analysis method to monitor the chemoconvulsant variation of total hemoglobin concentration and capillary CBV. As shown in Fig. 3a (right column), comparable neural activity was obtained between the baseline and seizure phases in the negative control group, and there was no significant gradual change of hemodynamics over time, demonstrating that the hemodynamic interferences were successfully rejected. Moreover, instantaneous blood flow perturbation due to heart beating would not affect the results, as every individual PA frame was compounded for two seconds that include 11–16 heart cycles of a rat (typically 5.5–8 beats per second).

The stability of stereotaxic fixation against the induced motor seizure were also investigated. The counter-hypothesis of this concern was an abrupt disorientation of rat brain due to motor seizure that will induce instantaneous decorrelation between adjacent PA frames. Also, based on the behavioral observation during seizure (Movie S4), we anticipated the decorrelation within a sub-second time scale, if it happened. For these hypotheses, we calculated the cross-correlation maps throughout PA frames obtained for 8 minutes (1920 frames, 240 frames/min). Three different time intervals were tested: 0.25 sec, 0.5 sec and 1 sec, which respectively correspond to 4, 2 and 1 frame intervals. For each interval, the minimal correlation projection (MCP) map was composed by finding the minimal value per pixel in temporal direction of the entire stack (Fig. S6). The PA frames with seizure indicated no significant decorrelation between adjacent PA frames compared to those obtained without seizure. Therefore, the interference by motor seizure could be rejected as potential cause of artifacts in the results.

Toxic CNS effects of VSD is another factor that can alter brain activity. We tested the protocols described in Fig. 1d with varying VSD concentration in rats as a direct application to the cortex (Fig. S7). Results for VSD IR780 with cortical application with cranial windows used in six male rats yielded reliable and reproducible EEG signatures using 10-min recordings for each concentration of IR780. This protocol identified that IR780 concentrations had no effect in altering the baseline EEG in the same rat, indicating no toxic effect on cortical circuit function. Direct cortical application with 100X IR780 resulted in significant EEG background suppression

in 4/6 rats, indicating that the certain concentrations of VSD could alter baseline circuit function in the motor cortex. This EEG suppression was recovered to baseline over the 10-min recording period, indicating that the transient effect from the time of application as the 100X VSD either diluted or cleared out of the focal application zone over the 10-min period.

Here, we demonstrated the first proof-of-concept of transcranial PA sensing of neural activity with near-infrared VSD, using a chemoconvulsant seizure model of the rat brain. We plan a number of follow-up efforts to further advance the concept. For instance, the use of localized, non-invasive neural stimulation will allow us to substantially expand our perspectives in real-time brain response to the external stimuli in a totally non-intrusive way.(28) In particular, we envisage that the integration with ultrasound neuromodulation may have a huge impact on the neuroscientific and clinical efforts by enabling the breakthrough beyond the passive brain investigation, while allowing additional benefits on non-pharmacological BBB opening.(29, 30) Furthermore, the neural sensing speed should be further improved. Current PA sensing speed is limited to 4 frames per second to obtain sufficient signal sensitivity in the deep brain cortex region with the current laser excitation scheme (20 Hz of pulse repetition rate, 3.5 mJ/cm^2). This speed may limit its applicability in research, as it is well known that the resting electrophysiological neural activity ranges up to several tens of Hz (e.g., delta: 1–4 Hz; theta: 4–8 Hz; alpha: 8–13 Hz; beta: 13–30 Hz; gamma: 30–50 Hz). (31) We will attempt to resolve the tradeoff in sensitivity by having ~100 Hz of sensing speed. Successful investigation will substantially increase the capability of the proposed approach for understanding brain function in real-time. In addition, we expect that improved signal processing for extracting neural activity from the ubiquitous blood context will enable better characterization of brain function. The present *in vivo* experiments confirmed the possibility of background suppression, but still have artifacts in the sensing area (Fig. 3a). Enhanced signal processing and/or use of multi-spectral wavelengths may allow significantly improved spectral unmixing of electrophysiological activities in the brain, leading to development of novel quantitative metrics for real-time brain characterization.

Methods

Fluorescence quenching-based near-infrared voltage-sensitive dye. Several cyanine VSDs have been proposed as markers for real-time electrical signal detection (32), and applied for optical imaging of the mitochondrial membrane potential in tumors (33) and fluorescence tracking of electrical signal propagation on a heart.(34) Recently we presented the mechanism of action of a cyanine VSD on the lipid vesicle model.(22) The discussed mechanism of VSD proposes a suppressive PA contrast when neuronal depolarization occurs, while yielding an enhancing contrast for fluorescence. In the present proof-of-principle study, we used the fluorescence quenching-based near-infrared cyanine VSD, IR780 perchlorate (576409, Sigma-Aldrich Co. LLC, MO, United States) with the analogous chemical structure of PAVSD800-2 in our previous study.(22) This VSD yields fluorescence emission leading to a reciprocal PA contrast with non-radiative relaxation of absorbed energy.

Photoacoustic imaging setup. For the recording of electrophysiological brain activities *in vivo*, an ultrasound research system was utilized that consisted of ultrasound array transducer (L14-5/38) connected to a real-time data acquisition system (SonixDAQ, Ultrasonix Medical Corp., Canada). To induce the PA signals, pulsed laser light was generated by a second-harmonic (532 nm) Nd:YAG laser pumping an optical parametric oscillator (OPO) system (Phocus Inline, Opotek Inc., USA). The tunable range of the laser system was 690-900 nm and the maximum pulse repetition frequency was 20 Hz. The laser pulse was delivered into the probe through bifurcated fiber optic bundles, each 40 mm long and 0.88 mm wide. The PA probe was located at around the Interaural 11.2 mm and Bregma 2.2 mm to obtain the cross-section of motor cortexes (Fig. S1). The energy density at skin surface was only 3.5 mJ/cm^2, which is far below the ANSI safety limit restricting the 5-ns pulsed laser exposure at 700 - 1400 nm of wavelength range to be lower than 20 mJ/cm^2.

Lipid vesicle phantom preparation for VSD validation. The lipid vesicle model was prepared using the same procedure as in Zhang et al (22); 25-mg soybean phosphatidyl-choline (type II) suspended in 1 mL of K+ buffer was used as the lipid vesicles. This vesicle contains 100 mM K_2SO_4 and 20 mM HEPES. The suspension was vortexed for 10 min, and followed by 60 min of sonication within bath-type sonicator to yield a translucent vesicle suspension. A Na^+ buffer was also prepared, which contains 100 mM Na_2SO_4 and 20 mM HEPES. Afterwards, approximately a 100∶1 K^+ gradient across vesicle membrane was established with 10 μL of lipid vesicle

suspension added to 1 mL of Na^+ buffer. In the vesicle phantom prepared, negative membrane potential (polarized state) was mimicked by adding 2.5 μL of 10 μM valinomycin—a K^+ specific ionophore, thereby K^+ ions were transported from inside to outside of vesicle membranes. Otherwise, 2.5 μL of 1 mM gramicidin, a nonspecific monovalent cation ionophore, enables Na^+ cations to move from outside to inside of vesicle membranes to short circuit the membrane potential (depolarized state). From these controls, our near-infrared VSD positively charged can move in and out through the vesicle membrane, leading to the change in fluorescence quenching depending on their aggregation status.

Estimation of quantum yield change of VSD. The quantum yields of the near-infrared VSD in depolarized states (Φ'_F) were estimated based on the Eq. 8 and 9 in our previous literature.(22) The ratio of absorbance and fluorescence emission in depolarized states (C_{abs} and C_F) were 0.97 and 0.60 compared to those in polarized states, respectively, and the estimated fractional changes of PA intensity were calculated for test quantum yields varying from 0 to 0.4 with 0.001 intervals. From the results, the optimal Φ'_F was chosen, for which the fractional change of PA intensity obtained in lipid vesicle phantom study was presented. The quantum yield in the polarized state (Φ_F) were also estimated by compensating for the absorbance and fluorescence emission changes when depolarized: $\Phi_F=(C_F/C_{abs})\,\Phi'_F$.

Animal preparation. For the proposed *in vivo* experiments. 8-9-week-old male Sprague Dawley rats weighing 275-390g were used (Charles Rivers Laboratory, Inc., MA, United States). The use of animals for the proposed experimental protocol was approved by the Institutional Research Board Committee of Johns Hopkins Medical Institute (RA16M225). All animals were anesthetized by intraperitoneal injection with a ketamine (100mg/ml) /xylazine (20 mg/ml) cocktail. (3:1 ratio based on body weight at 1ml/kg). The hair was shaved from the scalp of each rat for improved optical/acoustic coupling for transcranial PA recording. The head of the anesthetized rat was fixed to a stable position using a standard stereotaxic device. This fixation procedure was required to prevent any unpredictable movement during PA recording of neural activities.

Chemoconvulsant seizure induction. Penetylenetetrazole (PTZ), a gamma-aminobutyric acid (GABA) A receptor antagonist was used to induce acute seizures in the animals.(23) PTZ suppresses the inhibitory effects of GABA, thus leading to an easier and synchronized

depolarizations of neurons. (35-37) To induce global acute seizure in rat brain, an intraperitoneal (IP) injection of PTZ (45 mg/ml) was utilized based on the animal's body weight in a volume of 1ml/kg. Subsequent doses were given if no acute motor seizure was observed in 5-10 minutes after the first PTZ injection. Generally, 1-2 doses were sufficient to induce the motor seizures in our experiments.

Pharmacological treatment for VSD delivery into blood-brain barrier. The lumen of the brain microvasculature consists of brain endothelial cells, and the blood-brain barrier (BBB) is comprised of their tight junctions to control the chemical exchange between neural cells and cerebral nervous system (CNS). In this study, the penetration through BBB were achieved with a pharmacological method using FDA-approved regadenoson (Lexiscan, Astellas Pharma US, Inc. IL, United States). This modulates the Adenosine receptor signaling at BBB layer.(38) For our preliminary studies, the dosage and IV administration method indicated by the manufacturer was utilized. A volume of 150μl of the standard concentration of 0.08 mg/1ml was given to each animal regardless of the weight, followed by 150μl flush of 0.9% sodium chloride for injection. VSD penetration was expected during the Lexiscan's biological half-life, i.e., 2-4 minutes, thereby the experimental protocol was designed based on the pharmacological assumption.

***In vivo* experimental protocol.** The *in vivo* protocols were respectively designed for three experimental groups: negative control, control, and seizure groups. Fig. 1d shows the detailed protocol for each group to present the response to the administration of IR780, Lexiscan, and PTZ. Note that each data acquisition was performed for 10 min to cover the biological half-life of Lexiscan (2-3 min). Each dosing protocol of Lexiscan and VSD was as follows: through the jugular vein catheter port located in the neck, 150 μl of Lexiscan 0.4mg/5ml concentration was injected, and 300 μl of VSD was subsequently administrated at 0.1mg/ml concentration, followed by 150 μl of saline solution flush. The control and seizure groups were designed to distinguish the chemoconvulsant effects on neural activity: both groups received IR780 and Lexiscan, but only seizure group had intraperitoneal (IP) injection of PTZ (45mg/ml/kg). The induction of seizure was confirmed by monitoring motor seizure, and another dose of PTZ was injected intraperitoneally when no motor seizure was observed in 5-10 min. The negative control group was designed to validate the incapability of Lexiscan and PTZ to generate any bias on PA neural activity detection by excluding VSD administration. In the negative control group, first

data acquisition was conducted with the Lexiscan dosage, and the second data set was obtained during the chemoconvulsant seizure with Lexiscan dosage.

Criteria for selecting region-of-interest for STFT spectrogram. The regions-of-interest (ROI) were selected from left and right motor cortices in a PA image. The detailed criteria to select the appropriate ROI were as follows: (1) The minimal size of the ROIs on each hemisphere was set to 1.86 x 1.54 mm^2 included within the motor cortex region whose overall dimension is approximately 3 x 2.5 mm^2 based on the anatomy of the rat brain atlas shown in Fig. S1.(21) (2) The positions of ROIs were at least 2.75-mm below the scalp surface to avoid the regions of several other layers covering a brain, i.e., periosteum, skull, dura mater, arachnoid, subarachnoid space, and *pia mater*.(39) Following this criterion also allowed circumventing the dominant clutter signals from large vessels such as superior sagittal sinus (SSS) and superior cortical veins (SCV) nearby the dura mater, thereby the interference on neural activity response in PA signal was prevented.

Normalized time-frequency analysis. The real-time video of suppressive PA variation on motor cortex was reconstructed by expanding the ROI to cover the entire brain tissue region, and computing the localized STFT spectrogram for its segments (5 x 5 pixels, 18.6 x 19.3 μm^2 in dimension). The individual temporal frequency components of the STFT spectrograms were projected in the frequency domain to indicate the total amount of suppressive PA variation. To analyze this non-stationary PA intensity series in the time domain, the temporal analysis window was selected with 2-sec of time duration (40 samples) at the 0.5-sec interval, which enables the temporal frequency analysis up to 2Hz with the refreshing rate at 4Hz. Fig. S3 demonstrates the flow chart of our normalized time-frequency analysis to reconstruct the each STFT spectrogram representing PA fluctuation at different frequency. The processing consists of 4 steps for each segment as following:

1. **Step 1:** short-time Fourier transform of a segment;
2. **Step 2:** frequency normalization by the baseband intensity f_0 (i.e., 0.1 Hz): PA($\underline{t}, f$) = PA(t, f) / PA(t, f_0), where PA(t, f) and PA($\underline{t}, f$) are the PA sequence before and after temporal normalization;

3. **Step 3:** linear weighting of each temporal frequency component (i.e., 0.05 to 1 at 0.05 interval for 0 to 2 Hz temporal frequency component at 0.1Hz interval);
4. **Step 4:** temporal normalization to obtain $PA(\underline{t}, \underline{f}) = |PA(\underline{t}, f)/PA(\underline{t}, f_0)|$, in which the $PA_0(\underline{t}, f)$ was the averaged intensity during first 1 min after the VSD injection at each frequency component, f;
5. **Step 5:** Construction of the dynamic neural activity maps by allocating the averaged value of $PA(\underline{t}, \underline{f})$ in the frequency dimension at each time point.

Note that the linear weighting of each frequency component at Step 2 reflected the assumption that VSD responses fluctuating at higher frequency component indicates more vigorous neural activity, while signal component at lower frequency represent the consistent PA signal from blood context plus stationary VSD response in polarized state. Therefore, this procedure yields higher contrast resolution than pure VSD contrast between polarized and depolarized states (i.e., 12.22%, Fig. 2b) since it augments the fluctuating VSD responses, while suppressing the stationary signals. To derive the neural activity index of each rat shown in Fig 3b, 20 measurements for each rat have employed by dividing the temporal sequences of $PA(\underline{t}, \underline{f})$ in every 1 min duration (240 frames) for left/right motor cortexes to calculate the mean values and their standard variations.

EEG validation of neural seizure activity. To obtain the EEG records of electrical spike discharges that originated from motor cortex shown in Fig. 4, sub-dermal scalp EEG recording electrodes were located at the corresponding locations on motor cortex indicated by Xs in Fig. S7a, the schematic of the rat cranium (three electrodes, 1 recording and 1 reference over motor cortex, 1 ground electrode over rostrum). The EEG signal at motor cortex was recorded with the identical preparation procedures in PA imaging including animal preparation, administration of IR780, Lexiscan, and PTZ, time duration for recording, and interval between sequences in the protocol. Data acquisition was done using Sirenia software (Pinnacle Technologies Inc., Kansas, USA) with synchronous video capture. Briefly, the data acquisition and conditioning system had a 14-bit resolution, sampling rates of 400 Hz, high pass filters of 0.5 Hz and low pass filters of 60 Hz. The files were stored in .EDF format and scored manually for protocol stages using real time annotations added to the recording during the experiments. EEG power for 10 sec epoch displays within the scoring software package was done using an automated

module in Sirenia. Further details of our proposed EEG data acquisition and analysis used in this study are as presented in previous studies.(40, 41)

Validation of protocol for using sub-dermal EEG electrodes to determine toxic CNS effects of VSDs. VSDs effect on EEG signal from sub-dermal scalp electrodes was investigated in a pilot by direct cortical applications of increasing concentrations of VSDs in anesthetized rat with limited craniotomies while recording synchronous vEEGs (Fig S7). Increasing concentrations of VSD were tested in the same rat at temporally spaced time-points. Rats were anesthetized with IP injection to ketamine/xylazine and a cranial window made over the right motor cortex. After recording a baseline EEG in the rat for 10-min duration with the craniotomy, the follow-on EEG recording continued to record EEG following application of increasing concentrations of vehicle alone and VSD + vehicle for the same duration of EEG recordings (i.e.; 10 min) allowing comparisons of EEG responses to each increasing gradient of VSD on cortical activity as compared to baseline EEG signature in the same rat.

Acknowledgements

Authors thank Dr. Abhinav K. Jha for proofreading the manuscript and providing helpful comments. Also, authors thank Drs. Diane S. Abou and Daniel L. J. Thorek for providing equipment and facilities for *in vitro* experiments using a lipid vesicle model with helpful comments. Financial support was provided by the NIH Brain Initiative under Grant No. R24MH106083-03 and the NIH National Institute of Biomedical Imaging and Bioengineering under Grant No. R01EB01963.

References

1. Friston KJ (2009) Modalities, Modes, and Models in Functional Neuroimaging. *Science* 326(5951):399–403.

2. Frost JJ (2003) Molecular imaging of the brain: A historical perspective. *Neuroimaging Clinics of North America* 13(4):653–658.

3. Raichle ME, Mintun MA (2006) BRAIN WORK AND BRAIN IMAGING. *http://dxdoiorg/101146/annurevneuro29051605112819* 29(1):449–476.

4. Grillner S, et al. (2016) Worldwide initiatives to advance brain research. *Nat Neurosci* 19(9):1118–1122.

5. Roland PE, Hilgetag CC, Deco G (2014) Cortico-cortical communication dynamics. *Front Syst Neurosci* 8:19.

6. Vanitha NV (2011) Positron emission tomography in neuroscience research. *Annals of Neurosciences* 18(2):36.

7. Raichle ME (1998) Behind the scenes of functional brain imaging: a historical and physiological perspective. *Proc Natl Acad Sci USA* 95(3):765–772.

8. Vanitha NV (2011) Positron emission tomography in neuroscience research. *Annals of Neurosciences* 18(2):36.

9. Logothetis NK (2008) What we can do and what we cannot do with fMRI - ProQuest. *Nature*.

10. Berman MG, Jonides J, Nee DE (2006) Studying mind and brain with fMRI. *Social cognitive and affective neuroscience* 1(2):158–161.

11. Hillman EMC (2007) Optical brain imaging in vivo: techniques and applications from animal to man. *J Biomed Opt* 12(5):051402–051402–28.

12. Devor A, et al. (2012) Frontiers in optical imaging of cerebral blood flow and metabolism. *J Cereb Blood Flow Metab* 32(7):1259–1276.

13. Heo C, et al. (2016) A soft, transparent, freely accessible cranial window for chronic imaging and electrophysiology. *Sci Rep* 6(1):27818.

14. Strangman GE, Li Z, Zhang Q (2013) Depth sensitivity and source-detector separations for near infrared spectroscopy based on the Colin27 brain template. *PLoS ONE* 8(8):e66319.

15. Torricelli A, et al. (2014) Time domain functional NIRS imaging for human brain mapping. *NeuroImage* 85 Pt 1:28–50.

16. Wang LV, Hu S (2012) Photoacoustic tomography: in vivo imaging from organelles to organs. *Science* 335(6075):1458–1462.

17. Wang X, et al. (2003) Noninvasive laser-induced photoacoustic tomography for structural and functional in vivo imaging of the brain. *Nat Biotechnol* 21(7):803–806.

18. Deán-Ben XL, et al. (2016) Functional optoacoustic neuro-tomography for scalable whole-brain monitoring of calcium indicators. *Light Science Applications* 5(12):e16201–7.

19. Rao B, Zhang R, Li L, Shao J-Y, Wang LV (2017) Photoacoustic imaging of voltage responses beyond the optical diffusion limit. *Sci Rep* 7(1):S1–10.

20. American National Standard for the Safe Use of Lasers. (1975) American National Standard for the Safe Use of Lasers. *Annals of Internal Medicine* 82(1):132.

21. Paxinos G, Watson C (2014) *The Rat Brain in Stereotaxic Coordinates* (Elsevier Academic Press). Seventh edition Available at: https://books.google.com/books?id=FuqGAwAAQBAJ&printsec=frontcover#v=onepage&q&f=false.

22. Zhang HK, et al. (2017) Listening to membrane potential: photoacoustic voltage-sensitive dye recording. *J Biomed Opt* 22(4):045006.

23. Löscher W (2017) Animal Models of Seizures and Epilepsy: Past, Present, and Future Role for the Discovery of Antiseizure Drugs. *Neurochemical Research* 0(0):0–0.

24. Goldman H, Berman RF, Hazlett H, Murphy S (1992) Cerebrovascular responses to pentylenetetrazol: time and dose dependent effects. *Epilepsy Res* 12:227–242.

25. Nehlig A, et al. (1996) Absence seizures induce a decrease in cerebral blood flow: Human and animal data. *Journal of Cerebral Blood Flow and Metabolism* 16(1):147–155.

26. Hoshi Y, Tamura M (1993) Dynamic changes in cerebral oxygenation in chemically induced seizures in rats: study by near-infrared spectrophotometry. *Brain Res* 603(2):215–221.

27. Zhang T, et al. (2014) Pre-seizure state identified by diffuse optical tomography. *Sci Rep* 4(1):113–10.

28. Lewis PM, Thomson RH, Rosenfeld JV, Fitzgerald PB (2016) Brain Neuromodulation Techniques: A Review. *Neuroscientist*:1073858416646707.

29. Tufail Y, Yoshihiro A, Pati S, Li MM, Tyler WJ (2011) Ultrasonic neuromodulation by brain stimulation with transcranial ultrasound. *Nat Protoc* 6(9):1453–1470.

30. Chu P-C, et al. (2015) Neuromodulation accompanying focused ultrasound-induced blood-brain barrier opening. *Sci Rep* 5:15477.

31. Mantini D, Perrucci MG, Del Gratta C, Romani GL, Corbetta M (2007) Electrophysiological signatures of resting state networks in the human brain. *Proc Natl Acad Sci USA* 104(32):13170–13175.

32. Treger JS, Priest MF, Iezzi R, Bezanilla F (2014) Real-time imaging of electrical signals with an infrared FDA-approved dye. *Biophysj* 107(6):L09–L012.

33. Onoe S, Temma T, Shimizu Y, Ono M, Saji H (2014) Investigation of cyanine dyes for in vivo optical imaging of altered mitochondrial membrane potential in tumors. *Cancer Med* 3(4):775–786.

34. Martišienė I, et al. (2016) Voltage-Sensitive Fluorescence of Indocyanine Green in the Heart. *BPJ* 110(3):723–732.

35. Bradford HF (1995) Glutamate, GABA and epilepsy. *Progress in Neurobiology* 47(6):477–511.

36. de Boer T, Stoof JC, van Duijn H (1982) The effects of convulsant and anticonvulsant drugs on the release of radiolabeled GABA, glutamate, noradrenaline, serotonin and acetylcholine from rat cortical slices. *Brain Res* 253(1-2):153–160.

37. De Deyn PP, Macdonald RL (1989) Effects of antiepileptic drugs on GABA responses and on reduction of GABA responses by PTZ and DMCM on mouse neurons in cell culture. *Epilepsia* 30(1):17–25.

38. Carman AJ, Mills JH, Krenz A, Kim D-G, Bynoe MS (2011) Adenosine receptor signaling modulates permeability of the blood-brain barrier. *Journal of Neuroscience* 31(37):13272–13280.

39. Nowak K, et al. (2011) Optimizing a Rodent Model of Parkinson's Disease for Exploring the Effects and Mechanisms of Deep Brain Stimulation. *Parkinson's Disease* 2011(2754):1–19.

40. Adler DA, et al. (2014) Circadian cycle-dependent EEG biomarkers of pathogenicity in adult mice following prenatal exposure to in utero inflammation. *Neuroscience* 275:305–313.

41. Johnston MV, et al. (2014) Twenty-four hour quantitative-EEG and in-vivo glutamate biosensor detects activity and circadian rhythm dependent biomarkers of pathogenesis in Mecp2 null mice. *Front Syst Neurosci* 8(JUNE):118.

Figures

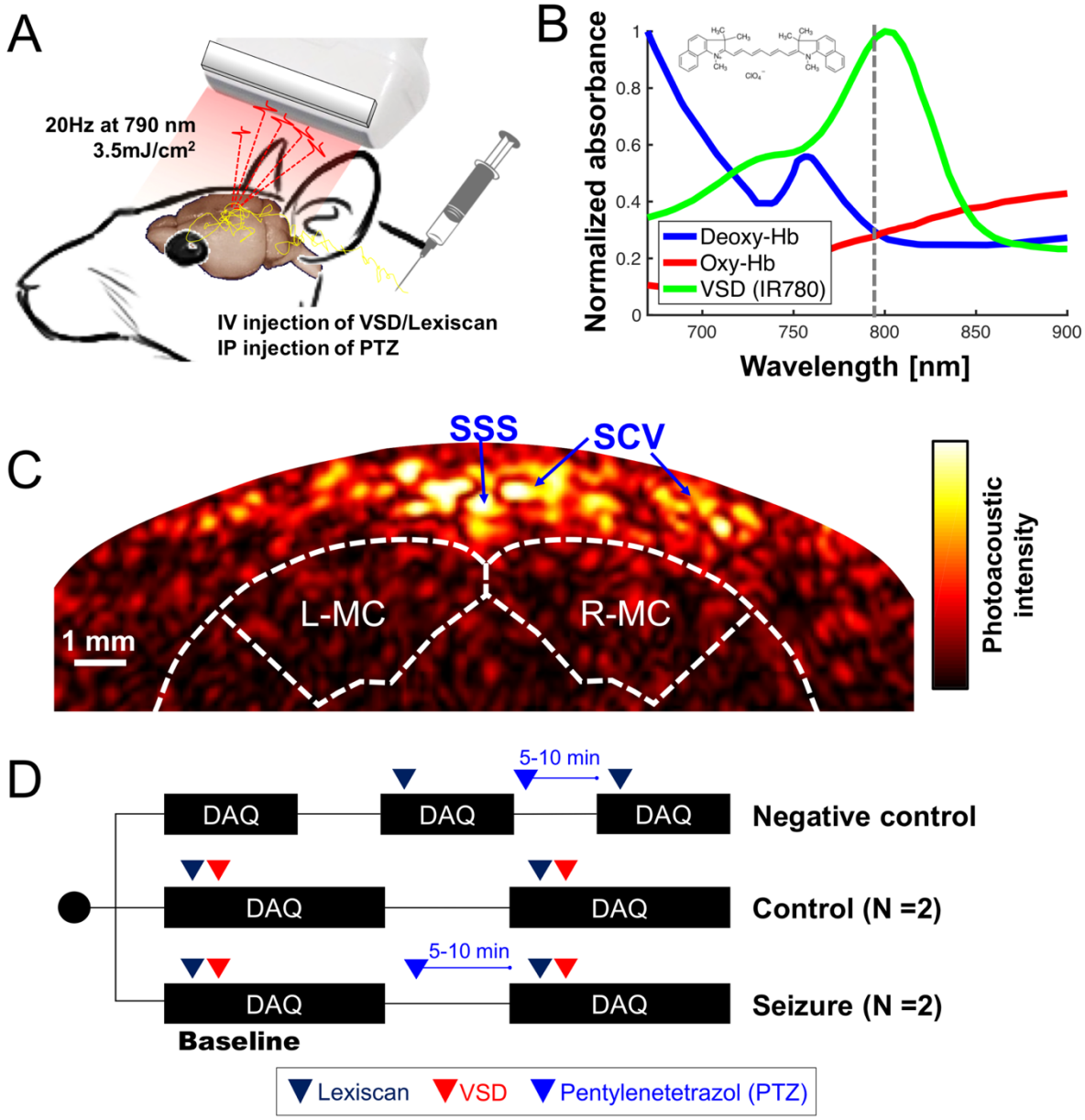

Fig. 1. Transcranial VSD sensing setup using PA imaging system: (A) schematic diagram of experimental setup; (B) absorbance spectra of VSD, deoxy- and oxy-hemoglobin. Dotted line indicates the wavelength used in *in vivo* experiment, i.e., 790 nm; (C) cross-sectional PA image of cerebral cortex; (D) *in vivo* experimental protocol. SSS: Superior sagittal sinus; SCV: Superior cortical veins. SSS: superior sagittal sinus; SCV: superior cortical veins; L-MC/R-MC: left/right motor cortex. Note that the outlines for brain and motor cortex in Fig. 1c was drawn based on the rat brain atlas (Interaural 11.2 mm, Bregma 2.2 mm, Fig. S1) (21)

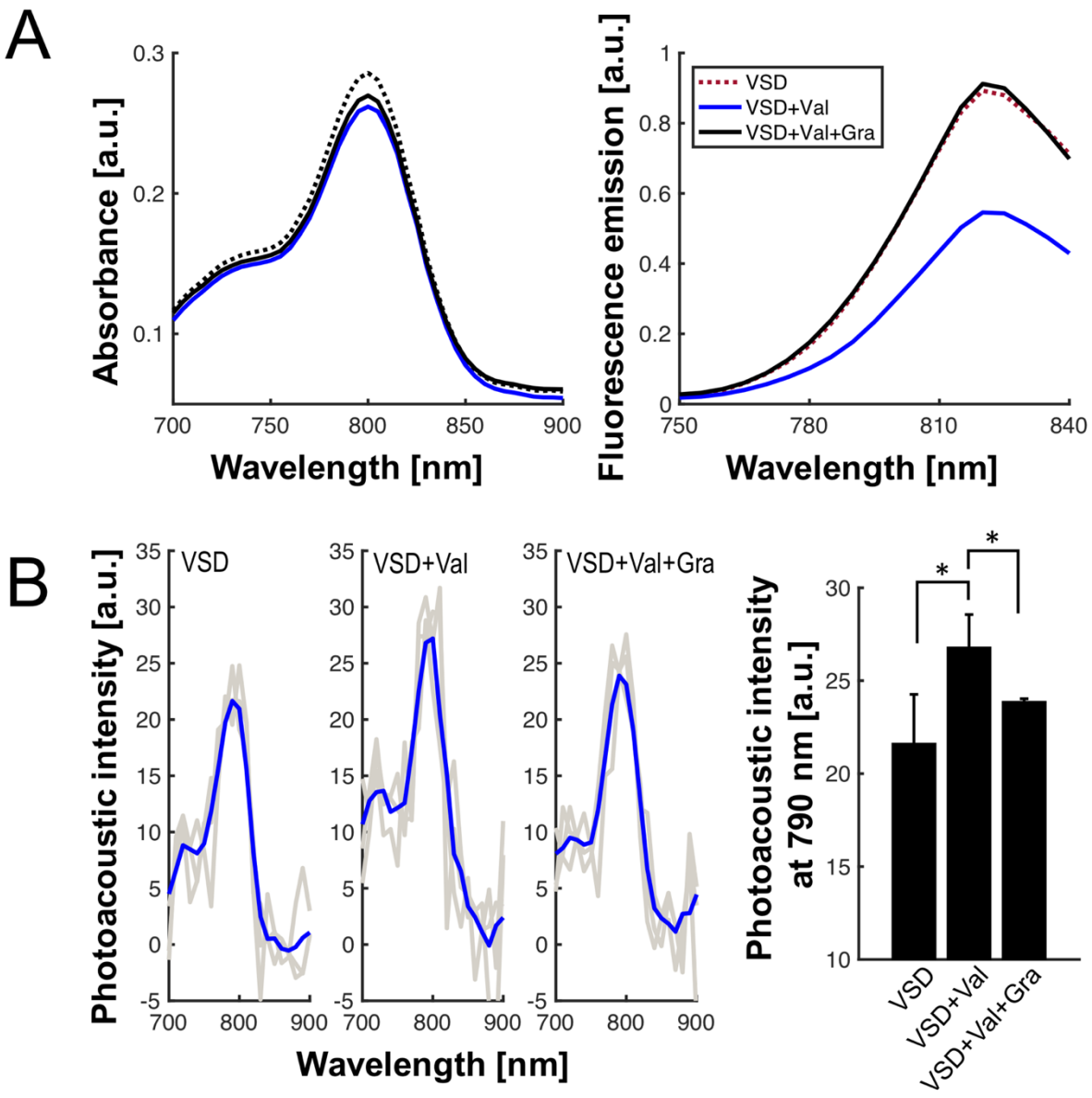

Fig. 2. Phantom experimental results using lipid vesicle membrane model with VSD. (A) Absorbance and fluorescence emission spectrum of near-infrared VSD. (B) Near-infrared photoacoustic spectrum and intensity change at the peak absorbance, i.e., 790 nm ($P < 0.0465$ for VSD vs. VSD+Val; $P < 0.0444$ for VSD+Val vs. VSD+Val+Gra). Val: valinomycin; Gra: gramicidin.

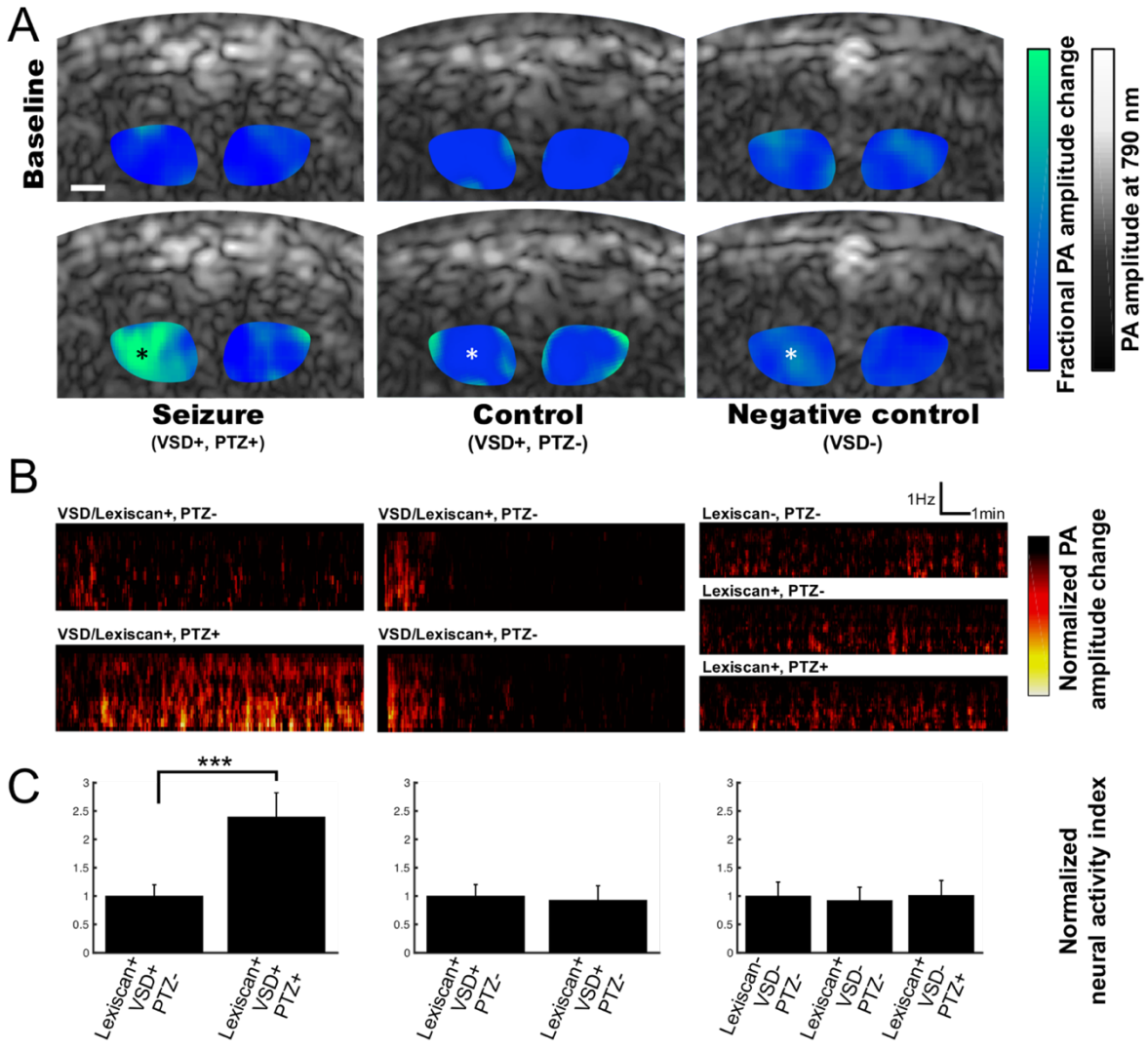

Fig. 3. The representative PA sensing of electrophysiological neural activity: (A) time-averaged neural activity maps and STFT spectrograms of VSD response of each protocol; and (B) neural activity index over 10 min in seizure, control, and negative control groups. Note that the regions-of-interest in the STFT spectrograms are indicated with asterisk marks in the respective neural activity map. The representative temporal evolution of neural activity map over time can be found in Movie S1, S2, and S3 for seizure, control, and negative control groups. Also, the neural activity index for each rat (i.e., rat 1, 4, and 5) is presented in Fig. S4. The neural activity index during seizure have been significantly differentiated from that in baseline phase ($P < 0.0001$). White bar in Fig. 3a indicates 1 mm.

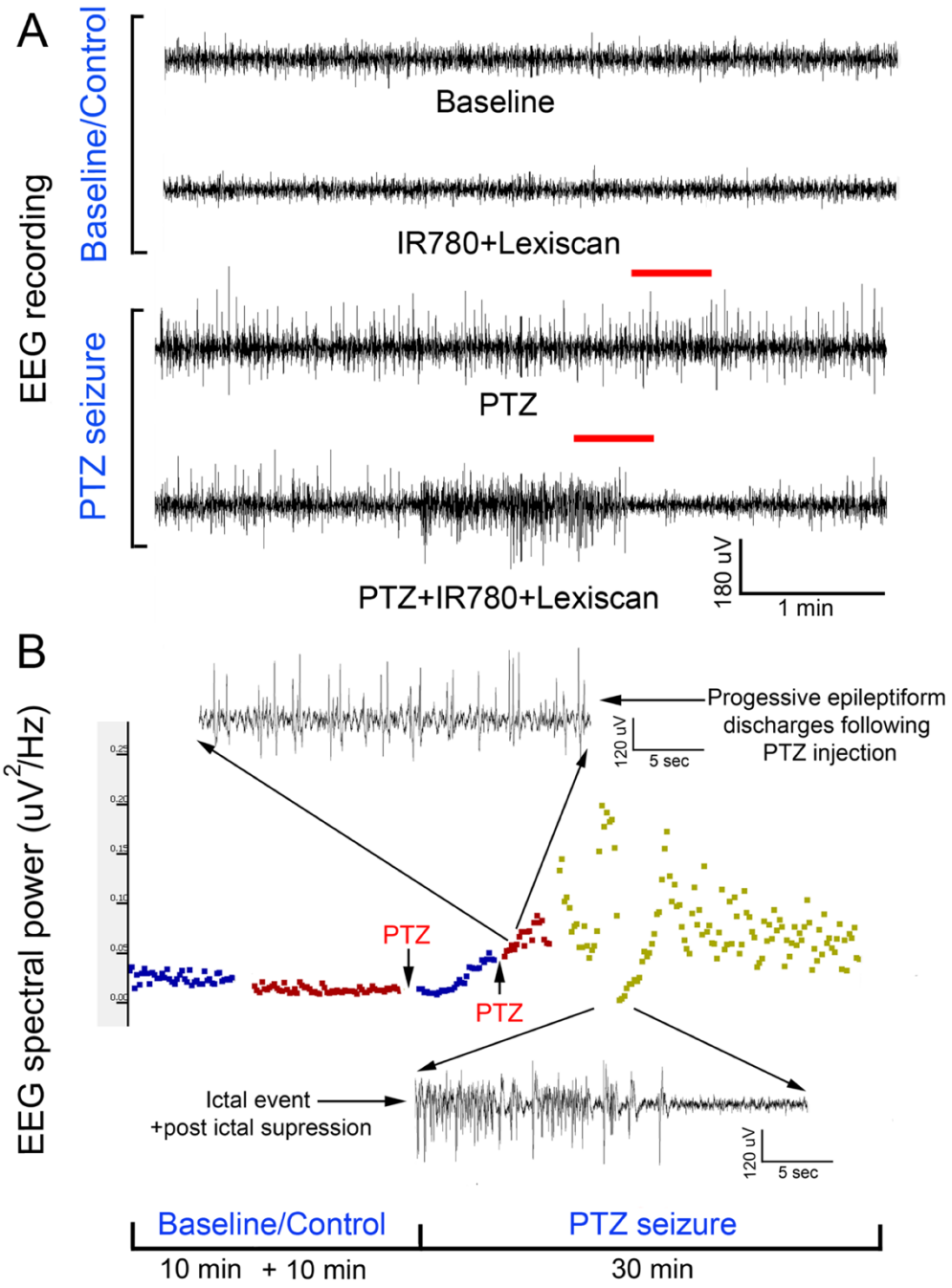

Fig. 4. Evolution of EEG signal in the *in vivo* protocol identical to transcranial PA imaging:

(A) Representative EEG traces recorded from rat motor cortex before and during induction of status epilepticus using chemoconvulsant PTZ. The baseline and control EEG traces represent EEG activity in an anesthetized rat (see methods) with and without IR780+lexiscan given at the dosage found to not alter baseline EEG activity in the pilot study. PTS seizure induction proceeded in classical style described previously wherein episodic epileptiform burst activity evolved into status epilepticus with intermittent occurrence of seizures and stable interictal

activity. (B) EEG spectral quantitation of the EEG recording done every 10 sec epoch during the EEG showed the expected progression in EEG power associated with evolution of the PTZ induced status epilepticus. Time line of PTZ injections indicated with arrows. Expanded EEG traces on top show the uniform epileptiform discharges after following second PTZ injection and below a seizure event followed of post-ictal suppression indicating the termination of that event.

Supplement information: Figures

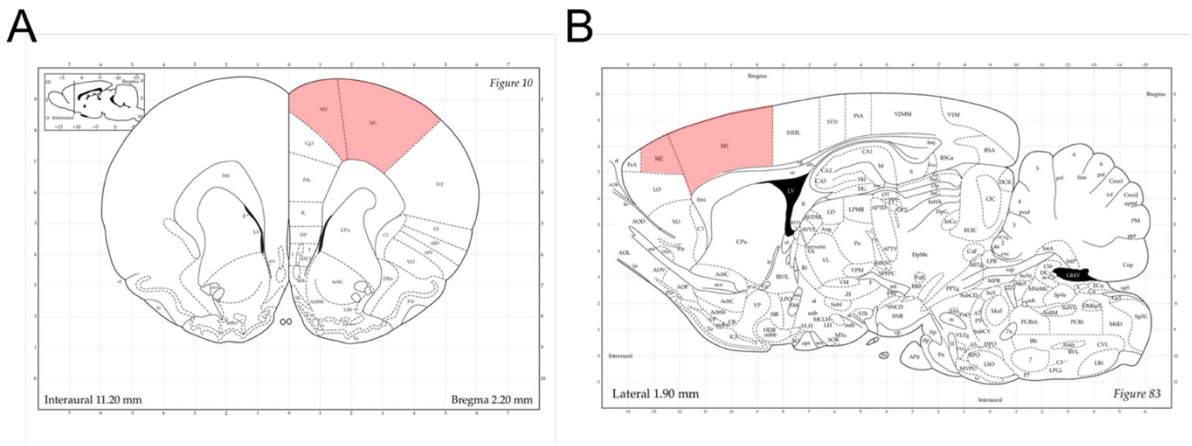

Fig. S1. Rat brain atlas for the region-of-interest for our experiments: [21] (A) coronal plane at interaural 11.2 mm and bregma 2.2 mm, (B) horizontal plane at lateral 1.9 mm. Note that the motor cortex, the target cortex-of-interest, are highlighted by red color. The permission for reproduction have been obtained from the publisher, Elsevier Academic Press.

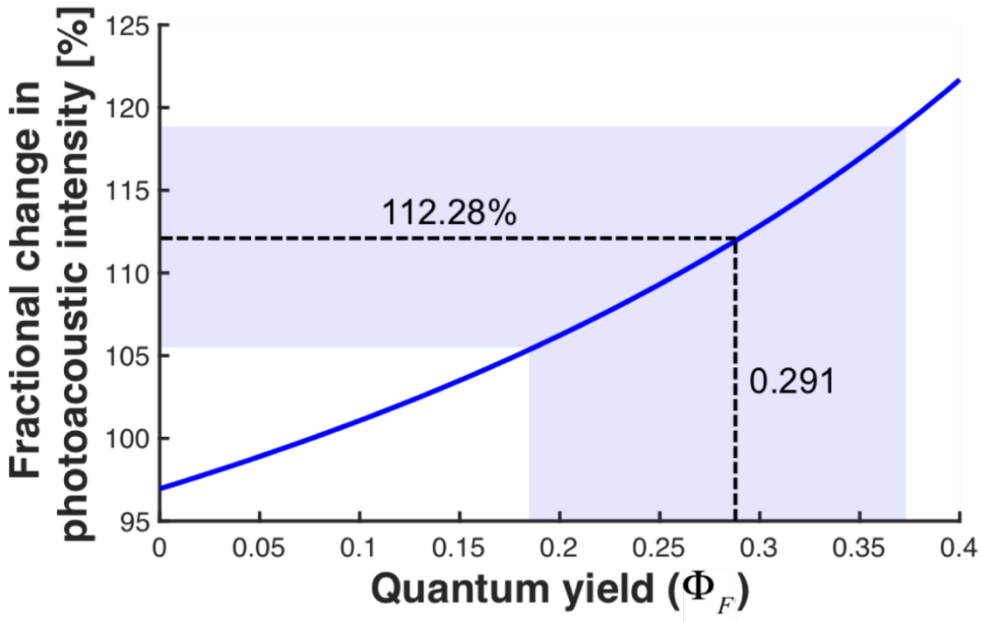

Fig. S2. Estimated quantum yield of near-infrared VSD: The equation in previous literature [22] was employed for the estimation of quantum yield using the fractional change of PA intensity and spectrophotometric measurements obtained by lipid vesicle experiment mimicking polarized/depolarized cell state (Fig. 2).

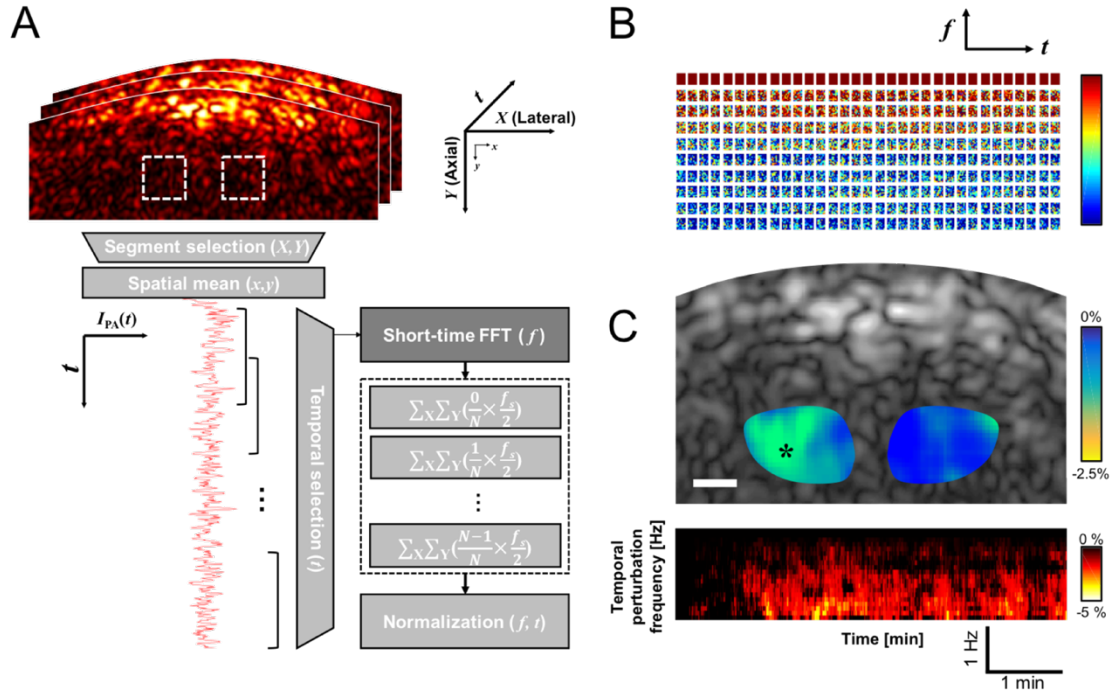

Fig. S3. Normalized time-frequency analysis method: (A) Flow chart of the proposed signal analysis; (B) Example of STFT segments in frequency and time domain; (C) Spatial-projected spectrogram for specific motor cortex region of interest; (D) Frequency-projected neural activity map for entire field-of-view. The white bar in Fig. S3c indicates 1 mm. (X, Y): lateral and axial indexes of a segment in PA image; (x, y): lateral and axial pixel indexes in each segment.

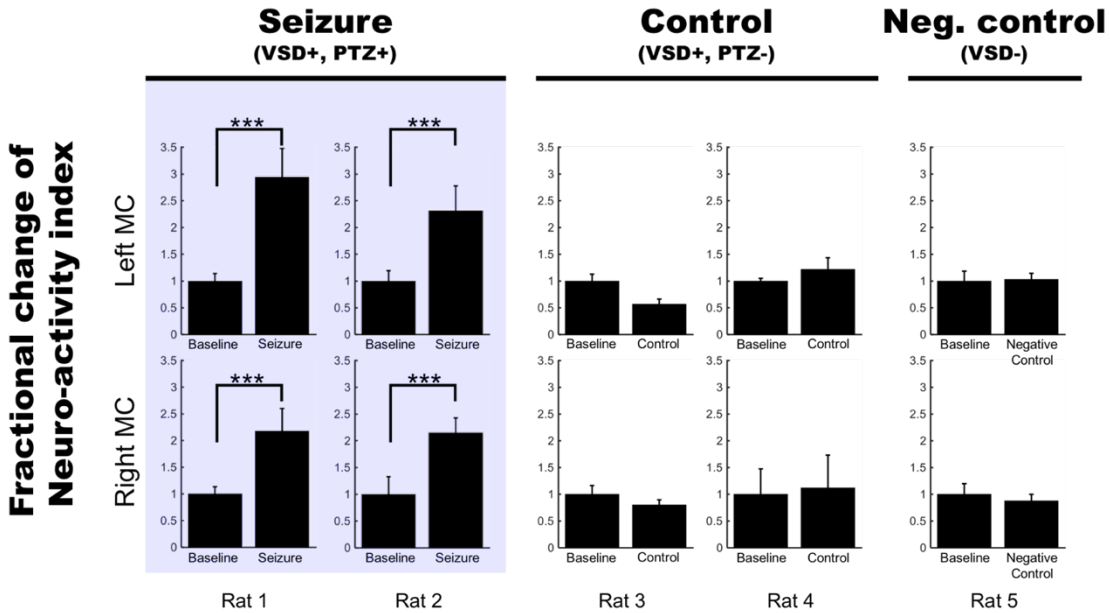

Fig. S4. Individual neural activity index for each rat in seizure, control, and negative control.

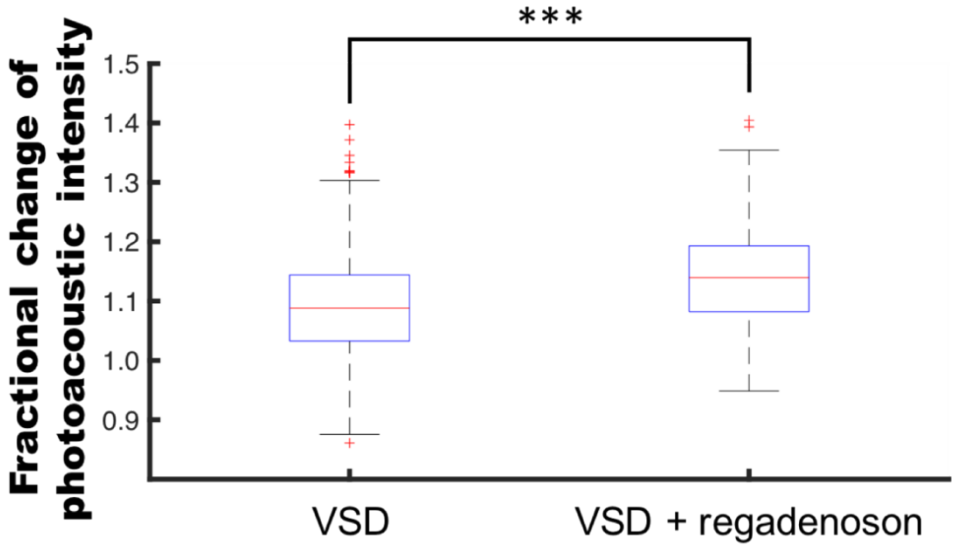

Fig. S5. Fractional changes of PA intensity depending on Adenosine receptor signaling modulation using intravenous regadenoson administration. Each PA sequences, i.e., VSD only and VSD+regadenoson, was measured from the brain tissue region (3 mm below the skin surface), and projected during last 2 min (8-10 min, 480 times points).

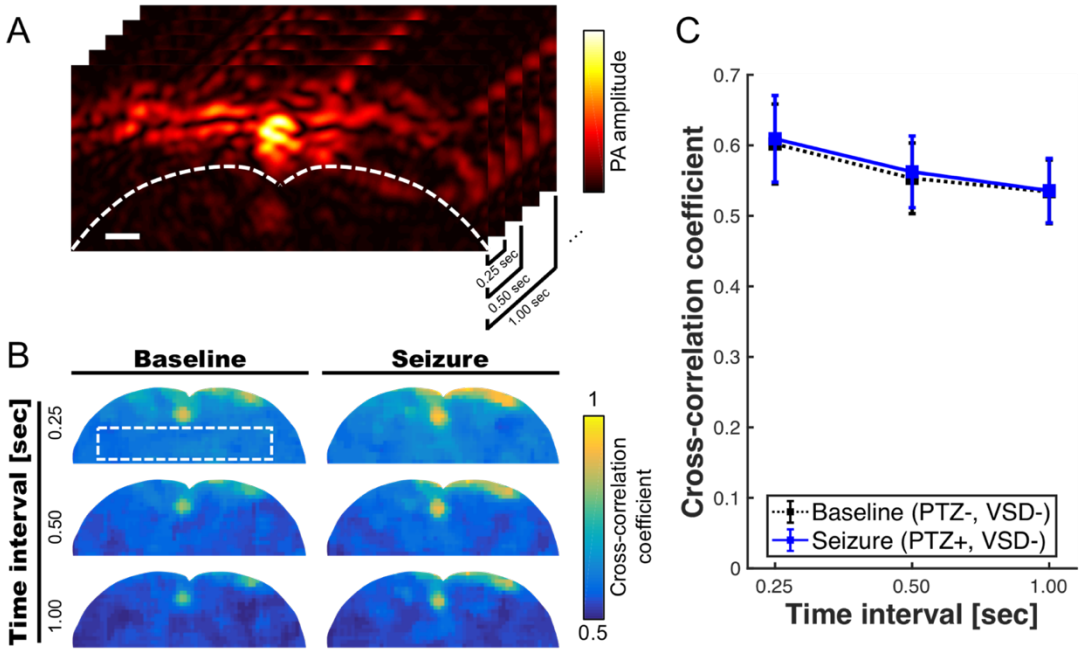

Fig. S6. Minimal correlation projection (MCP) image using cross-correlation coefficients with varying time interval, i.e., 0.25 sec, 0.5 sec, and 1 sec, which respectively corresponds to 1, 2, 4 frame intervals with the imaging rate at 4 frames per second. (A) region of interest for the inter-frame cross-correlations, (B) MAP images of baseline (PTZ-, VSD-) and seizure groups (PTZ+, VSD-) for brain tissue region. (C) Cross-correlation coefficient for varying time intervals.

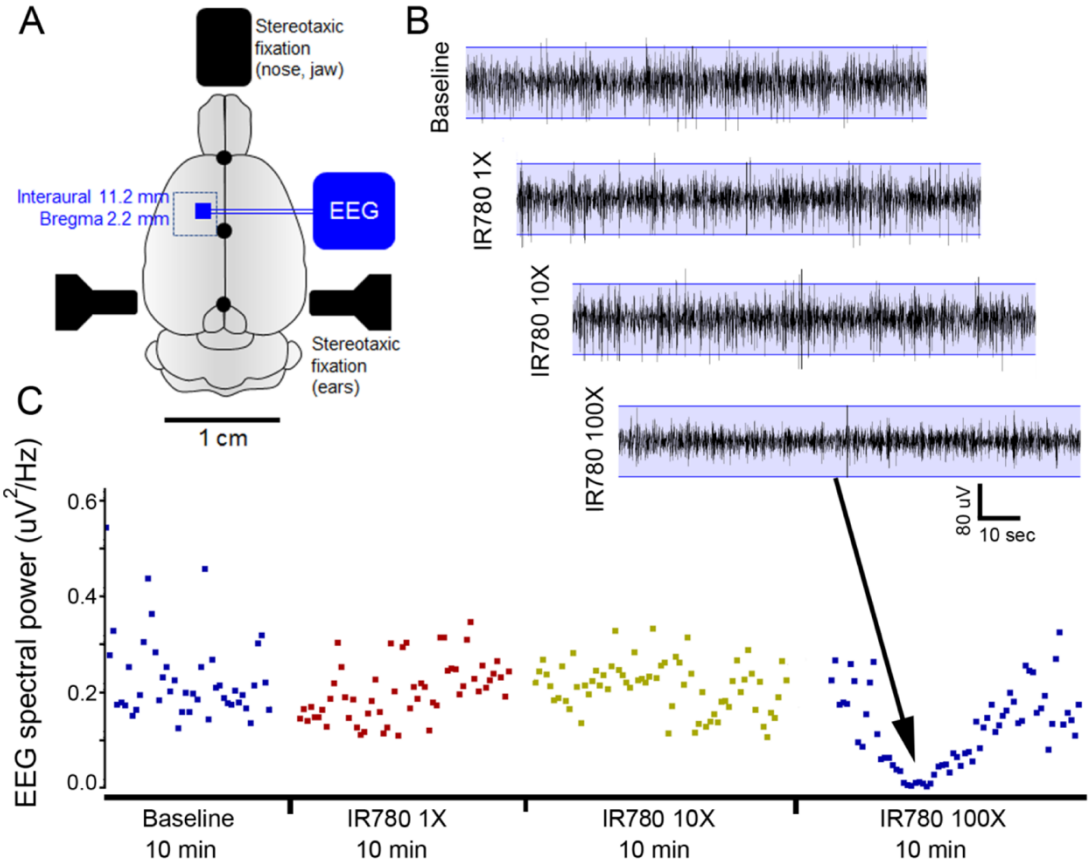

Fig. S7. VSD toxicity study using EEG recordings during direct cortical applications using a cranial window in rats. (A) Schematic of experimental protocol. A rectangular cranial window drilled under anesthesia overlying unilateral motor cortex. Duramater was kept intact. Following craniotomy, a small window was made in duramater without traversing blood vessels. (B) EEG recording of baseline brain activity under anesthesia was followed by using a hamilton micro syringe to apply increasing concentrations of IR780 directly to the cortical surface via window made in duramater. Base EEG remained unaltered at lower concentrations but showed significant background suppression after applying a 100X solution. This study allowed us to determine the concentration of IR780 10X for all PA experiments. (C) EEG power spectral quantification for every 10-sec epoch of EEG over the duration of the recording confirmed EEG suppression with the 100X dose.

Supplement information: Movies

Movie S1. The representative PA sequence: seizure group:

https://drive.google.com/open?id=0BzuzZg6RZcGoS2hTUTBGblBTWHc

Movie S2. The representative PA sequence: control group:

https://drive.google.com/open?id=0BzuzZg6RZcGodDl5Z1lsNGlHeWM

Movie S3. The representative PA sequence: negative control group:

https://drive.google.com/open?id=0BzuzZg6RZcGoNUJ3TGNRWDBvSkU

Movie S4. The tonic-clonic movements in the fore and hind-limbs of the anesthetized rat:

https://drive.google.com/open?id=0BzuzZg6RZcGoUktvZXNRelAxMFU

Movie S5. The representative PA video of neural activity map in seizure group:

https://drive.google.com/open?id=0BzuzZg6RZcGobTJROFJRWjd3Q3c

Movie S6. The representative PA video of neural activity map in control group:

https://drive.google.com/open?id=0BzuzZg6RZcGobE5tZUtEblJOdW8

Movie S7. The representative PA video of neural activity map in negative control group:

https://drive.google.com/open?id=0BzuzZg6RZcGoVlR4UkRHRktFa1k